Maximum Torque Output Strategy of a Bearingless Induction Motor in the Field-Weakening Region

Wenxin Fang[1], Zebin Yang[1, *], Xiaodong Sun[2], and Guangxin Wang[1]

Abstract—In order to realize the maximum torque output (MTO) in the field-weakening region for a bearingless induction motor (BIM) stator vector control, a flux feedforward control strategy is proposed. Firstly, based on the restrictions of the stator flux oriented control and the dynamic characteristics of the current in the BIM field-weakening region, the optimal distribution of the torque current and excitation current and the dynamic model of the maximum torque output strategy are analyzed. Then, the field-weakening region could be divided into two parts according to the change of slip. It can be proved that the BIM works under the voltage and current limitations in the field-weakening region I, and works under the voltage and torque limitations in the field-weakening region II. By this way, the optimal flux mathematical model of the BIM can be obtained. Finally, the MTO in the field-weakening region is proved. The simulation and experiment results show that the proposed flux feedforward control strategy in the field-weakening region can make the output torque and current tracking effect improve significantly when the BIM runs beyond the rated speed. At the same time, the good suspension performance of the BIM is realized.

1. INTRODUCTION

A bearingless motor is a special motor, which has frictionless wear, corrosion resistance, no lubrication, and can realize "self-suspension operation" [1–5]. Compared with other motors, a bearingless induction motor (BIM) possesses the advantages of simple structure, solid and reliable, uniform air gap, low cost, and low groove pulsation torque. A new electrical transmission scheme is provided for the development of sophisticated transmission equipment, such as high-speed centrifugal pump, flywheel energy storage, and agricultural equipment [6–10].

In the oriented flux vector control system of the bearingless induction motor powered by the inverter [11–14], when the BIM works below the rated speed, the motor flux can be kept constant, and its maximum output torque [15–17] is only limited by the rated current and the maximum current of the inverter; when the motor speed exceeds the rated speed, it enters the field-weakening region. With the increase of the counter electromotive force of the rotor winding, the output voltage of the inverter will be limited, which affects the maximum torque output of the motor. Therefore, various methods about the field-weakening region have been proposed by the domestic and foreign scholars [18–21]. In [22], a field-weakening control algorithm based on the maximum torque-current ratio is proposed, which is controlled by checking the table of the maximum torque-current ratio in the constant torque, and the torque command is generated by the field weakening algorithm in the constant power region. This method realizes the high-speed operation of the motor when the current and voltage limits are not exceeded. In [23], the voltage components during the steady high-speed operation are analyzed through the voltage equation. The stator resistance voltage drops; the dynamic current term and dynamic

flux linkage term are ignored based on the rotational speed and excitation current which are inversely proportional method; the adjustment range of the motor speed is widened. Reference [24] controls the motor stator closed-loop voltage, current limit, and the angle difference between the stator flux and rotor flux, which are through the control strategy of the stator closed-loop voltage, so that the motor maximum torque can be output in the field-weakening region. This method can reduce the influence of DC side voltage changes, which makes the largest steady-state torque generated in the entire field weakening range and has fast dynamic response ability. But this method needs to add control variables, so the control algorithm will be more complicated. In order to ensure the motor operated efficiently and stably when the speed exceeds the rated speed, the maximum torque output strategy adopted in the field weakening region is particularly important. As a special type of motor that the functions of suspension and rotation are integrated, BIM has a coupling effect between the torque winding and suspension winding [25–27]. Therefore, in order to make the BIM more stable during high-speed operation, the research on the maximum torque control in the field-weakening region is carried out.

In this paper, based on the BIM mathematical model, a strategy for maximum torque output in the oriented stator field weakening region is proposed. First, based on the restrictions of the stator flux and the dynamic characteristics of the current in the BIM field-weakening region [28–30], the voltage, current, and torque limitation were analyzed. Secondly, according to the Γ-type equivalent circuit of BIM [31], the field weakening region is divided into two parts: field weakening region I and region II. By this circuit, The BIM works in the voltage and current limit in the field-weakening region I and works in the voltage and torque limit the field-weakening region II are proved, so the corresponding optimal magnetic flux can be obtained. Therefore, the maximum torque can be output in the field weakening area, and the rotor can be suspended well. Finally, the feasibility and effectiveness of the proposed method are verified by simulation and experiments.

2. MATHEMATICAL MODEL OF BIM

The torque winding with a pole pair of P_1 and the suspension force winding with a pole pair of P_2 are wound on the stator of the BIM simultaneously. The following three conditions [32] are satisfied by these two sets of windings to realize the effective suspension operation of the motor:

(1) $P_1 = P_2 \pm 1$;

(2) Electrical angular frequency $\omega_1 = \omega_2$;

(3) The direction of the generated rotating magnetic field is the same.

The interaction of the currents in the two sets of windings is used to control the uneven distribution of the air gap magnetic field of the BIM, thereby a controllable radial force is generated acting on the rotor to achieve suspension.

The generation principle of radial suspension force in the BIM is shown in Fig. 1. The 4-pole torque winding and 2-pole suspension force winding are stacked in the stator slots. In the no-load state,
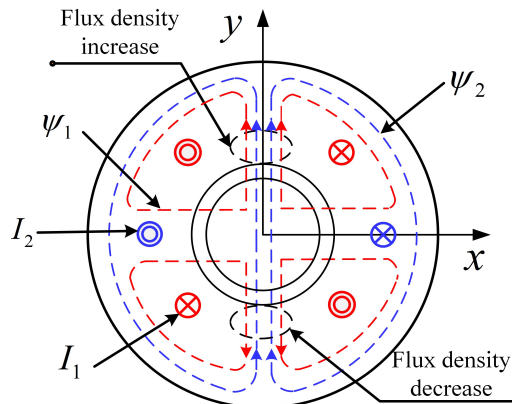

Figure 1. Generation principle of radial suspension force in the BIM.

currents I_1 and I_2 are passed through the two sets of windings, respectively, and the flux linkages ψ_1 and ψ_2 are generated as shown in Fig. 1. ψ_1 and ψ_2 are in the same direction on the upper side of the air gap, so the air gap magnetic density increases, while ψ_1 and ψ_2 on the lower side are opposite, so the air gap magnetic density decreases, thereby a radial suspension force F_y is generated along the positive direction of the y-axis. Similarly, if we want to obtain the radial suspension force along the x-axis, we can pass a current perpendicular to I_2 in the suspension force winding. Therefore, the magnitude and direction of the suspension force can be controlled by the current in the suspension force winding, and the stable suspension of the BIM rotor can be realized.

3. LIMITATION OF THE BIM OPERATION IN THE FIELD-WEAKENING REGION

3.1. The Voltage and Current Limits

The steady-state voltage equation of the BIM in the stator field-oriented vector control system is:

$$
\begin{aligned}
u_{sd} &= R_s i_{sd} + p\psi_{sd} - \psi_{sq} p\theta_r \\
u_{sq} &= R_s i_{sq} + p\psi_{sq} - \psi_{sd} p\theta_r
\end{aligned}
\tag{1}
$$

where u_{sd}, u_{sq} represent the stator voltage; i_{sd}, i_{sq} represent the stator current on the d-axis and q-axis, respectively; ψ_{sd} and ψ_{sq} represent the components of the stator flux on d-axis and q-axis, respectively; R_s is the stator resistance per phase.

Thus, the motor terminal voltage amplitude can be obtained as follows:

$$
|u_s| = \omega_r |\psi_s|
\tag{2}
$$

The stator flux linkage vector ψ_s and stator current i_s are crossed to the electromagnetic torque of the BIM:

$$
T_e = \frac{3}{2} n_p \psi_s \times i_s = \frac{3}{2} n_p |\psi_s| |i_s| \cos\phi_e
\tag{3}
$$

where $\cos\phi_e$ is the power factor.

It can be seen from Eq. (2) that when the amplitude of the stator flux linkage is a constant value, the amplitude of the motor terminal voltage increases proportionally with the increase of the rotational speed. However, the vector control system is driven by an inverter composed of power semiconductor, so the stator winding current and terminal voltage must be limited. The constraints are:

$$
|i_s| = \sqrt{i_{sd}^2 + i_{sq}^2} \leq I_{s\max},
\tag{4}
$$

$$
|u_s| = \sqrt{u_{sd}^2 + u_{sq}^2} \leq U_{s\max}
\tag{5}
$$

where $I_{s\max}$ and $U_{s\max}$ are the maximum current and voltage amplitudes allowed by the stator winding, respectively.

The speed of the BIM cannot increase infinitely under the condition of constant stator flux linkage amplitude, due to the limitation of the maximum stator winding terminal voltage. When the speed of
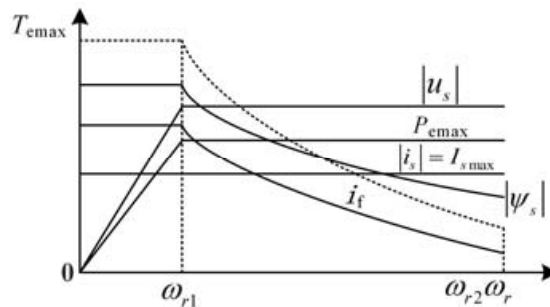

Figure 2. Field-weakening control characteristics of the BIM.

motor reaches the rated electrical angular velocity, the stator terminal voltage amplitude reaches the limited value, that is $\omega_{r1}|\psi_s| = U_{s\,\max}$. At this point, if the speed is required to continue to increase, the stator flux linkage amplitude $|\psi_s|$ must be reduced, so that the motor terminal voltage is still maintained at $U_{s\,\max}$. Fig. 2 shows the motor characteristics under the field-weakening control.

3.2. The Torque Limit

The out-of-step torque and torque equations under the BIM stator field-oriented vector control are as follows:

$$T_e \leq \frac{3(1-\sigma)n_p}{4\sigma L_s}\psi_s^2 \tag{6}$$

$$T_e = \frac{3}{2}n_p\psi_s i_{sq} \tag{7}$$

where n_p is the number of pole pairs, which can be obtained according to the above two equations:

$$i_{sq} \leq [(1-\sigma)\psi_s]/(2\sigma L_s) \tag{8}$$

The range of the q-axis component of the stator current under torque limit control is shown in Eq. (8). If the q-axis current command exceeds this range, the motor cannot run stably. The range of the torque limit is affected by the leakage inductance coefficient and magnetic flux command: if the magnetic flux command is constant, the leakage inductance coefficient is inversely proportional to the range of the torque limit, and the magnetic flux command is proportional to the range of the torque limit.

3.3. Division of the Field-Weakening Region

When the BIM is under stator field control, the extreme torque is limited. The analysis with the T-type equivalent circuit is relatively complicated, but the torque characteristics of the motor can be deduced more directly through its Γ-type equivalent circuit under the directional control of the stator field. In: $L_M = L_s$, $L_L = \frac{L_s L_{1s}}{L_m} + \frac{L_s^2 L_{1r}}{L_m^2}$, $R_R = L_s^2 R_r/L_m^2$. From the Γ-type equivalent circuit shown in Fig. 3, the stator current and rotor current equation can be obtained as follows:

$$I_s = \frac{U_s\left[R_R + js\omega_e\left(L_L + L_M\right)\right]}{-s\omega_e^2 L_L L_M + j\omega_e L_M R_R}, \tag{9}$$

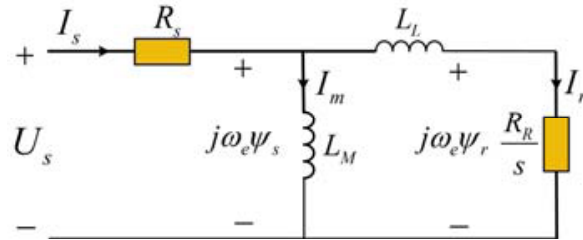$$I_r = \frac{U_s}{j\omega_e L_L + R_R/s} \tag{10}$$

Figure 3. The Γ equivalent circuit of the BIM.

Therefore, the electromagnetic power and torque of the motor are as follows:

$$P_M = \frac{3}{2}\frac{|U_s|^2 R_R}{s\left(\omega_e L_L\right)^2 + R_R^2/s}, \tag{11}$$

$$T_M = \frac{3}{2}\frac{n_p|U_s|^2 R_R}{s\omega_e\left(\omega_e L_L\right)^2 + \omega_e R_R^2/s} \tag{12}$$

where $|U_s|$ is the peak value of the stator phase voltage, due to $s\omega_e(\omega_e L_L)^2 + \omega_e R_R^2/s \geq 2\omega_e^2 L_L R_R$. According to Eq. (12), when the slip ratio is shown as in (13), the maximum torque of BIM is as follows:

$$s_m = R_R/(\omega_e L_L),\tag{13}$$

$$T_{M\max} = \frac{3n_p U_s^2}{4\omega_e^2 L_L}\tag{14}$$

The slip ratio in Eq. (13) is the maximum slip ratio of the motor, and the torque in Eq. (14) is the out-of-step torque of the motor. When the motor just enters the field-weakening region, because the extreme current is limited, the slip rate of the motor is usually less than the maximum slip rate, and the actual torque is also less than the out-of-step torque. So this area is defined as the field-weakening region I.

When the actual slip s of the motor is equal to the maximum slip s_m, the torque output by the motor is the out-of-step torque. As shown in Eq. (14), this region is defined as the field-weakening region II.

In Fig. 4, the solid lines are the mechanical characteristic curves of the motor at different synchronous speeds, and the dotted line is the maximum torque that the motor can output when it runs at different synchronous speeds. Due to the limitation of the current, the slip ratio of the motor is less than the maximum slip ratio, and the output torque is less than the maximum torque in the mechanical characteristics in the field-weakening region I. With the increase of the speed, the motor enters the field-weakening region II. At this point, the slip ratio is the maximum slip ratio, and the output torque is the out-of-step torque.
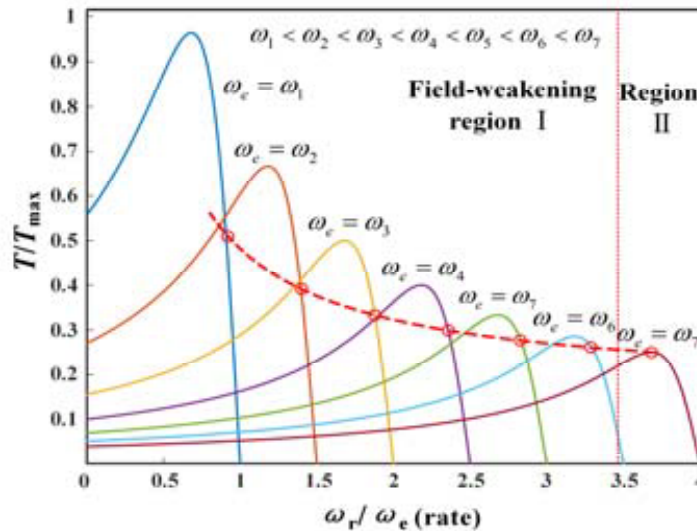

Figure 4. The torque characteristics of the BIM in the field weakening region.

4. MAXIMUM-TORQUE-OUTPUT TRAJECTORY OF THE BIM IN FIELD-WEAKENING REGION

In order to make full use of the inverter capacity, the motor needs to work at the current limit and voltage limit at the same time to ensure that it can output the maximum torque in the field-weakening region. When the motor is running in the field-weakening region II, it always works at the maximum slip s_m point to ensure the stable operation of the motor, and at the same time, the motor needs to work at the voltage limit in order to obtain the maximum torque output.

4.1. Analysis of the BIM Characteristics in the Field-Weakening Region I

According to the Γ-type equivalent circuit, the impedance angle of the BIM can be derived:

$$\angle Z = \arctan\left[\frac{\left(\dfrac{R_R}{\omega_{s1}}\right)^2 L_M + L_M L_L \left(L_M + L_L\right)}{L_M^2 R_R/\omega_{s1}}\right] \tag{15}$$

In Eq. (15):

$$\omega_{s1} = R_R\sqrt{\frac{\omega_e^2 L_M^2 - (U_{\max}/I_{\max})^2}{(U_{\max}/I_{\max})^2 \left(L_M + L_L\right)^2 - \omega_e^2 L_M^2 L_L^2}} \tag{16}$$

where ω_{s1} is the slip angular frequency.

Let $R_R/\omega_{s1} = x$, then Eq. (15) can be rewritten as:

$$\angle Z = \arctan\left[\frac{x}{L_M} + \frac{L_L \left(L_M + L_L\right)}{L_M x}\right] \tag{17}$$

When $0 < x < \sqrt{L_L(L_M + L_L)}$, the impedance angle of the motor keeps decreasing; on the contrary, the impedance angle of the motor keeps increasing. When $x = \sqrt{L_L(L_M + L_L)}$, Eq. (16) has a unique minimum value, and its value is:

$$\angle Z = \arctan\left[\frac{2\sqrt{L_L \left(L_M + L_L\right)}}{L_M}\right] \tag{18}$$

At this point, the synchronous angular velocity is:

$$\omega_{ec} = \frac{U_{\max}}{I_{\max}}\sqrt{\frac{(L_M + L_L)^2 + L_L \left(L_M + L_L\right)}{L_M^2 L_L^2 + L_L L_M^2 \left(L_M + L_L\right)}} \tag{19}$$

4.2. Analysis of the BIM Characteristics in the Field-Weakening Region II

In order to ensure the stable operation of the motor, it must work at the maximum slip s_m point in the field-weakening region II, and in order to obtain the maximum torque output, the motor needs to work at the voltage limit at the same time. At this point, the motor runs at the maximum slip rate ω_{s1m} stably. The maximum slip value can be obtained from Eq. (13), as shown below:

$$\omega_{s1\,\max} = s_m \omega_e = \frac{R_R}{L_L} \tag{20}$$

From Eqs. (16) and (20), the turning frequency in the field-weakening region II can be obtained as follows:

$$\omega_{ec2} = \frac{U_{\max}}{I_{\max}}\frac{1}{L_M L_L}\sqrt{\frac{1}{2}[(L_M + L_L)^2 + L_L^2]} \tag{21}$$

The optimal voltage vector trajectory based on the maximum torque output equation is shown in Fig. 5. The blue line is the optimal strategy trajectory; the green line is the voltage limit trajectory; and the red line is the current limit trajectory. As can be seen from the figure, with the speed increasing, the current limit range becomes larger. In the base-speed region, with the speed increasing, the optimal trajectory moves from point 0 to point A. When the motor speed is higher than the base speed, the motor enters the field-weakening region. Then the optimal trajectory moves between two points AB, and finally stays at point B, at this point $|u_{sd}| = \psi_{sq}$.
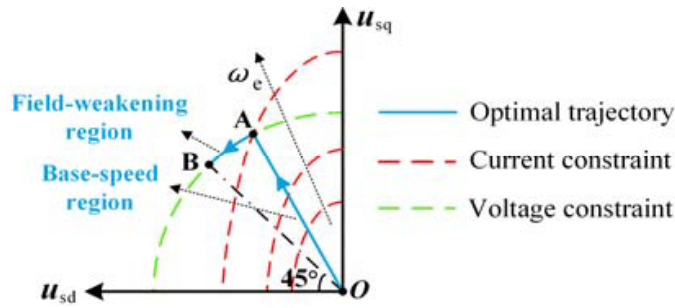
Figure 5. Optimal vector trajectory in the field-weakening region of the BIM.

4.3. Flux Feedforward Control Strategy for Field-Weakening Operation

The reference value of the flux linkage and torque is adjusted online according to the inverse proportional rule under the flux feedforward control strategy for field-weakening operation, and the speed regulation range of the motor can be expanded by this means. The method is to make the reference magnetic flux inversely proportional to the motor speed, and by this method, the rated speed can be exceeded by the motor actual speed. Therefore, when the rated speed is exceeded, the reference magnetic flux is adjusted as follows:

$$\psi_s^* = \psi_s^{\text{rated}} \frac{\omega_{\text{rated}}}{\omega_m} \tag{22}$$

When the rated speed is exceeded, the maximum torque output capacity will be decreased according to the reduced magnetic flux:

$$\hat{T}_e = \hat{T}_e^{PI} \frac{\omega_{\text{rated}}}{\omega_m} \tag{23}$$

At this point, the equation of the decoupling term i_{dq} of the motor is:

$$i_{dq} = \frac{L_s \sigma i_{sq}^2}{\psi_s - \sigma L_s i_{sd}} \tag{24}$$

The control block diagram of the flux feedforward control strategy in the field-weakening region of the bearingless induction motor in the stator magnetic field is shown in Fig. 6. The estimated values of the speed and angle are obtained by the adaptive flux observer.
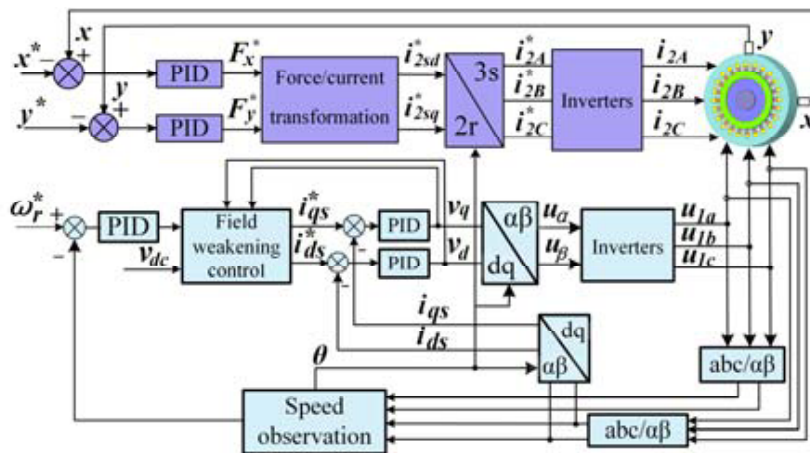

Figure 6. Control block diagram of the system.

5. SIMULATION AND EXPERIMENT RESULT

In order to verify the effectiveness of the flux feedforward control strategy in the field-weakening region of the bearingless induction motor in the stator magnetic field that is proposed in this paper, a simulation model of the control system is built and simulated by Matlab/simulink. The parameters of the BIM are shown in Table 1.

Table 1. The parameters of the BIM.

Parameters	Torque winding	Suspension winding
Core length (mm)	105	105
Rotor mass (kg)	2.85	2.85
Rotational inertia (kg·m^2)	0.00769	0.00769
Rated power (w)	1000	500
Rated current (A)	2.86	2.86
Rotor resistance (Ω)	11.48	0.075
Mutual inductance of stator and rotor (H)	158.56	9.32
Self-inductance of stator and rotor (mH)	209.79	12.32
Rotor leakage inductance (mH)	9.22	5.42
Stator leakage inductance (mH)	4.45	2.67

5.1. Running under Load

During the acceleration process of the bearingless induction motor from 0 to 4500 r/min with a load of 3 N·m, the flux feedforward control method proposed in this paper and traditional control method in which the magnetic flux is inversely proportional to the rotational speed are compared in the field-weakening region. The comparison curves are shown in Fig. 7. It can be seen from the figure that in
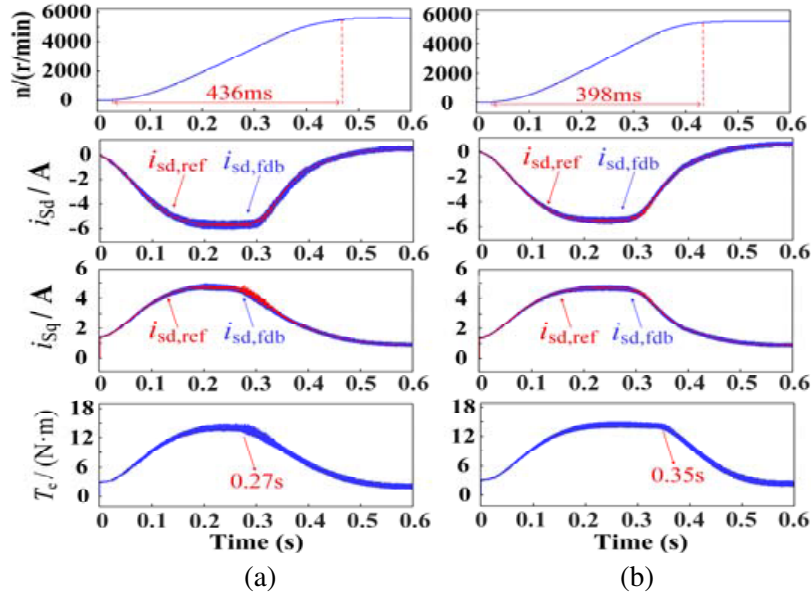

Figure 7. Acceleration process from 0 rpm to 4500 rpm under load operation of the BIM. (a) Conventional method. (b) Proposed method.

the constant torque region, the setting value can be well tracked by the stator d and q axis currents under the control of the two methods, and the torque can also be kept in a stable state.

However, when the motor exceeds the rated speed of 1500 r/min and enters the field-weakening region, the actual and the given values of stator d and q-axis currents will deviate significantly under the traditional control method shown in Fig. 7(a). At 0.27 s, there will be a significant drop, and the fluctuation will be large. With the motor under flux feedforward control in Fig. 7(b), the given and the actual values of the stator d and q axis currents deviation is significantly reduced; the torque decreases at 0.35 s; and the torque can always maintain the state of the maximum torque. The accelerate time of the motor under the control of the traditional method and the method proposed in this paper are 436 ms and 398 ms, respectively. Therefore, the flux feedforward control method proposed in this paper has obvious advantages.

Figures 8 and 9 are the radial displacement curves of the rotor. It can be seen from the figures that after the BIM enters field-weakening region, the displacement of the rotor is much smaller than the air gap value of the BIM by 0.4 mm, and it still has good suspension characteristics.
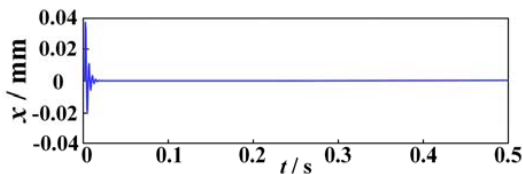

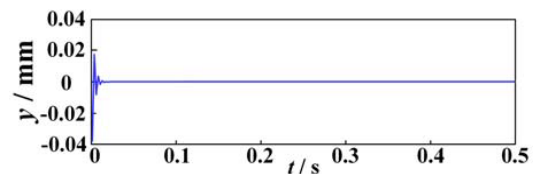**Figure 8.** Rotor offset in x-direction.

Figure 9. Rotor offset in y-direction.

5.2. Running under Speed Reference Piecewise Changes

In order to make a more comprehensive analysis, under the speed reference piecewise changes, the use of the flux feedforward control strategy is compared with the traditional control strategy in which the flux is inversely proportional to the rotational speed. As shown in Fig. 10, in Fig. 10(a), the three-stage accelerate times of the motor speed are 122 ms, 178 ms, and 235 ms, respectively. It can be seen from Figs. 10(b), 10(c), and 10(d) that during the first stage of speed increase, because the motor is in the
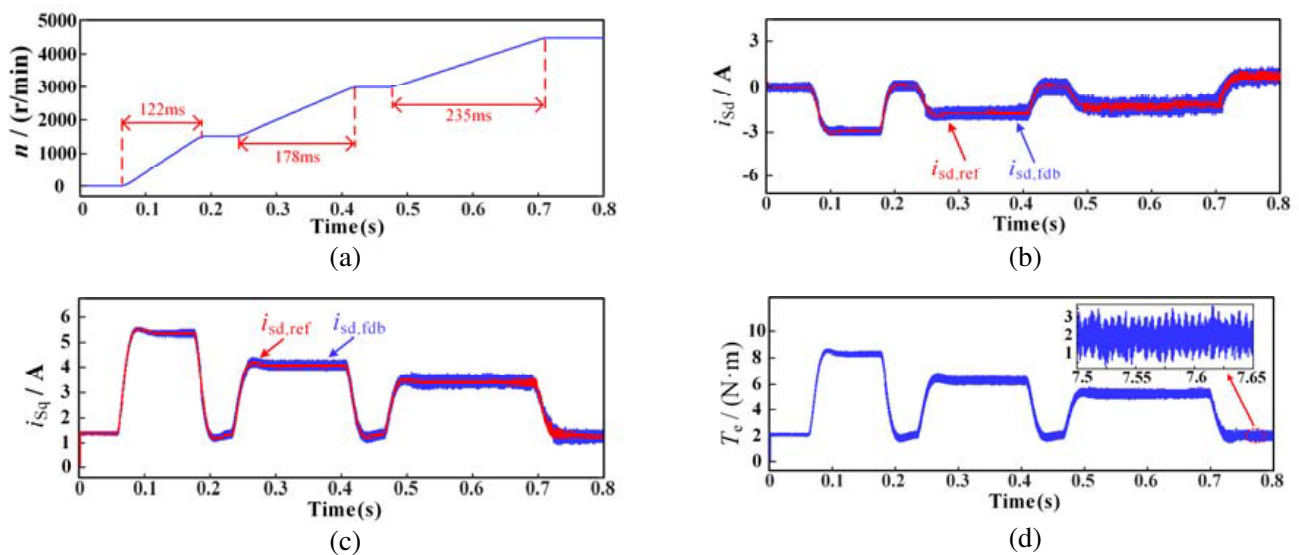

Figure 10. Step acceleration process from 0 to 4500 r/min under conventional method of the BIM. (a) Speed accelerate curve. (b) Exciting current curve. (c) Torque current curve. (d) Output torque curve.

base-speed region, the reference value can be tracked well by i_d and i_q, and the torque fluctuation is stable. At 0.24 s, the speed changes from 1500 to 3000 r/min, and the BIM enters the field-weakening area I. At this point, the deviations of i_d, i_q and the reference value are widened obviously, and the torque fluctuation is also significantly larger. Then at 0.48 s, the speed changes from 3000 to 4500 r/min, and the BIM enters the field-weakening region II. It can be seen from the figure that the deviations of i_d, i_q and the reference value are enlarged constantly. From the enlarged view of Fig. 10(d), when the motor runs stably at 4500 r/min, the torque fluctuation can be controlled within ±1 N·m.

The simulation curve under the flux feedforward control is shown in Fig. 11. When the speed rises from 0 to 1500 r/min, the motor stays in the base-speed region, so the accelerate time is 122 ms, which is consistent with the traditional method; then, step changes from 1500 to 3000 r/min in 150 ms; finally, step changes 3000 to 4500 r/min in 207 ms. Compared with the traditional method, the acceleration time is significantly shortened. In Figs. 11(b) and 11(c), the deviations of i_d, i_q and the reference value are significantly reduced compared with the traditional method in Fig. 10, and the change of the reference value is relatively smooth. In Fig. 11(d), when the speed is finally maintained at 4500 r/min, the torque fluctuation can be controlled within ±0.5 N·m from the enlarged figure, so the current reference value can be tracked better by the method proposed in this paper, and the motor can be run more efficiently.
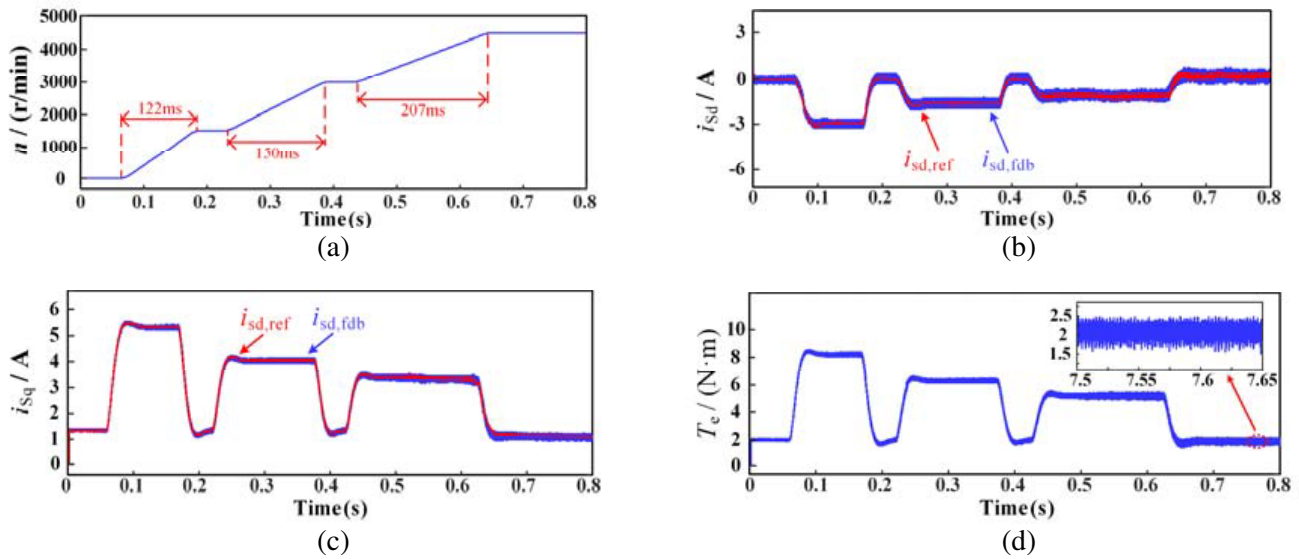

Figure 11. Step acceleration process from 0 to 4500 r/min under proposed method of the BIM. (a) Speed accelerate curve. (b) Speed accelerate curve. (c) Speed accelerate curve. (d) Speed accelerate curve.

5.3. Experimental Verification

In order to further verify the effectiveness of the proposed flux feedforward control strategy in field-weakening region, the digital system experimental platform is used as shown in Fig. 12, which is developed by our research group independently. The experimental motor parameters are consistent with the simulation ones. IGBT is used as the switch tube of the experimental platform, and the sampling frequency is set to 20 kHz. In order to observe and record the experimental waveforms and data conveniently, the rotational speed and radial displacement are output to the oscilloscope for display through D/A.

When the actual speed increases from 0 to 4500 r/min, the experimental curves of the rotational speed, phase "a" current, and rotor displacement which are controlled by flux feedforward control in the field-weakening region are shown in Figs. 13–15. Fig. 13 shows the rotational speed compared result between traditional method and proposed method. It can be seen from the figure that when the motor speed accelerates from 0 to 4500 r/min, the BIM under traditional method needs 1.33 s, while under
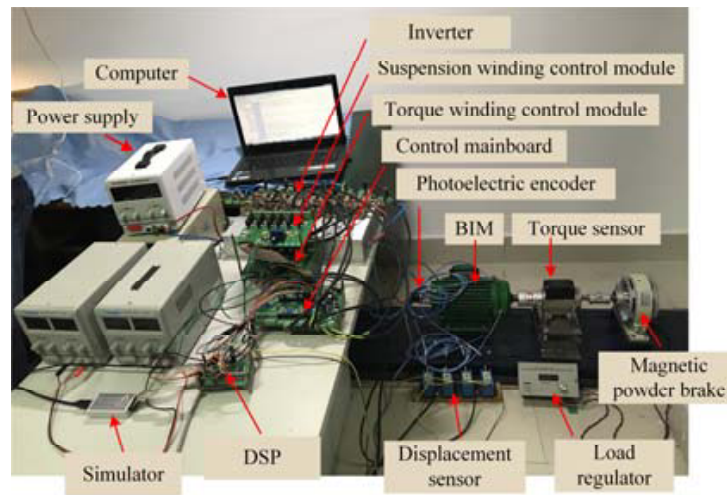
Figure 12. Experimental platform.
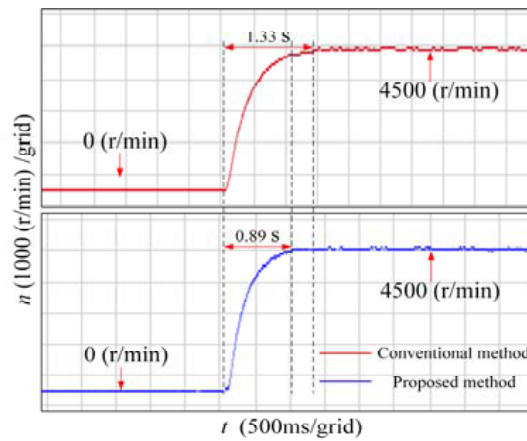

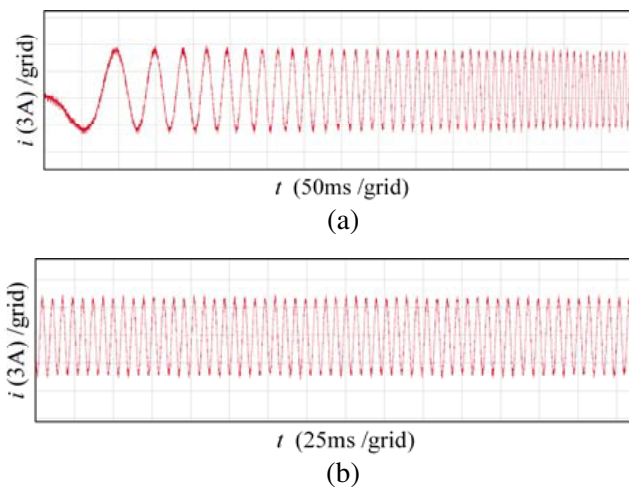**Figure 13.** Speed acceleration diagram of the BIM.

Figure 14. The "a" phase current diagram of the BIM. (a) The diagram of "a" phase current when the speed increases. (b) The diagram of "a" phase current at 4500 r/min.

the proposed method it only needs 0.89 s, and the jitter is smaller when the speed reaches 4500 r/min. The experimental comparison shows that under the proposed method in this paper, the motor speed can rise faster, and the fluctuation is decreased. It can be seen that the experiment results in Fig. 13 are consistent with the simulation ones in Fig. 7, which proves the feasibility of the proposed method.

Figure 14 is the current experimental diagram under the flux feedforward control in field-weakening region. In Fig. 14(a), the current amplitude is 5 A in the stage of acceleration; when the motor reaches the maximum speed, the current jitter amplitude is decreased and still maintains a sinusoidal operation, which can be seen from Fig. 14(b).

The experimental diagram of the rotor displacement when the motor operates at the maximum speed is shown in Fig. 15. It can be seen from the figure that the rotor shakes slightly when the rated speed is exceeded, but it is much smaller than the air gap value of the motor by 0.4 mm, which can realize the good suspension performance. The experimental results are consistent with the simulation ones. Therefore, the proposed flux feedforward control in the field-weakening region can realize the motor's stable operation, and the proposed method has certain feasibility.
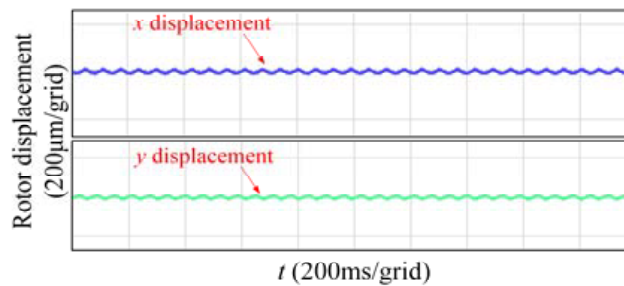

Figure 15. Rotor displacement of the BIM.

6. CONCLUSION

In this paper, the maximum torque output control strategy in the field-weakening region is proposed. The effectiveness and practicability of the proposed method are proved by theoretical analysis, simulated and experiment results, and two conclusions are obtained as follows:

(1) The variation process of slip and torque is deduced when the BIM operates in the field weakening region, which is based on the Γ-type equivalent circuit and constraints of the BIM when it operates in the field weakening region. The field-weakening region is divided to two regions by the slip variation, then the torque output in the above two regions is the maximum torque, and the corresponding flux is the optimal are proved.

(2) In order to meet the conditions of field-weakening operation, the proportional factor of flux linkage and torque is introduced into the maximum torque output strategy. When the actual speed is higher than the base speed by 300%, the field-weakening operation is realized, and stable operation of the BIM is guaranteed.

REFERENCES

1. Noh, M. and D. L. Trumper, "Homopolar bearingless slice motor with flux-biasing Halbach arrays," *IEEE Transactions on Industrial Electronics*, Vol. 67, No. 9, 7757–7766, 2020.
2. Sun, X. D., Z. J. Jin, Y. F. Cai, Z. B. Yang, and L. Chen, "Grey wolf optimization algorithm based state feedback control for a bearingless permanent magnet synchronous machine," *IEEE Transactions on Power Electronics*, Vol. 35, No. 12, 13631–13640, 2020.
3. Liu, G., Z. Ma, H. Zhu, J. Sun, and J. Huan, "Multi-objective optimization and analysis of six-pole outer rotor hybrid magnetic bearing," *Progress In Electromagnetics Research C*, Vol. 119, 97–114, 2022.

4. Yang, Z. B., C. L. Lu, X. D. Sun, J. L. Ji, and Q. F. Ding, "Study on active disturbance rejection control of a bearingless induction motor based on an improved particle swarm optimization-genetic algorithm," *IEEE Transactions on Transportation Electrification*, Vol. 7, No. 2, 694–705, 2021.

5. Wang, H. J. and F. X. Li, "Design consideration and characteristic investigation of modular permanent magnet bearingless switched reluctance motor," *IEEE Transactions on Industrial Electronics*, Vol. 67, No. 6, 4326–4337, 2020.

6. Yang, Z. B., Q. F. Ding, X. D. Sun, and C. L. Lu, "Design and analysis of a three-speed wound bearingless induction motor," *IEEE Transactions on Industrial Electronics*, 2021, doi: 10.1109/TIE.2021.3128900.

7. Jin, Z. J., X. D. Sun, and Z. B. Yang, "A novel four degree-of- freedoms bearingless permanent magnet machine using modified cross feedback control scheme for flywheel energy storage systems," *International Journal of Applied Electromagnetics and Mechanics*, Vol. 60, No. 3, 379–392, 2019.

8. Bu, W. S., F. Zhang, F. Z. He, L. G. Sun, and Y. K. Qiao, "Neural network inverse system decoupling fuzzy self-tuning proportional-derivative control strategy of a bearingless induction motor," *Proceedings of The Institution of Mechanical Engineers. Part I — Journal of Systems and Control Engineering*, Vol. 235, No. 7, 1113–1124, 2021.

9. Xu, T., Z. Yang, X. Sun, and J. Jia, "Electromagnetic property analysis of a bearingless induction motor using amorphous alloy material," *Progress In Electromagnetics Research M*, Vol. 104, 49–59, 2021.

10. Sinervo, A. and A. Arkkio, "Rotor radial position control and its effect on the total efficiency of a bearingless induction motor with a cage rotor," *IEEE Transactions on Magnetics*, Vol. 50, No. 4, 1–9, 2014.

11. Yang, Z. B., Q. F. Ding, X. D. Sun, H. M. Zhu, and C. L. Lu, "Fractional-order sliding mode control for a bearingless induction motor based on improved load torque observer," *Journal of the Franklin Institute-Engineering and Applied Mathematics*, Vol. 358, No. 7, 3701–3725, 2021.

12. Yao, H., Y. Yan, T. N. Shi, G. Z. Zhang, Z. Q. Wang, and C. L. Xia, "A novel SVPWM scheme for field-oriented vector-controlled PMSM drive system fed by cascaded H-bridge inverter," *IEEE Transactions on Power Electronics*, Vol. 36, No. 5, 8988–9000, 2021.

13. Sun, X. D., B. K. Su, L. Chen, and Z. B. Yang, "Precise control of a four degree-of-freedom permanent magnet biased active magnetic bearing system in a magnetically suspended direct-driven spindle using neural network inverse scheme," *Mechanical Systems and Signal Processing*, Vol. 88, 36–48, 2017.

14. Khoury, G., R. Ghosn, F. Khatounian, M. Fadel, and M. Tientcheu, "Energy-efficient field-oriented control for induction motors taking core losses into account," *Electrical Engineering*, 2021, doi: 10.1007/s00202-021-01321-6.

15. Zhang, X., B. Wang, Y. Yu, J. Zhang, J. X. Dong, and D. G. Xu, "Analysis and optimization of current dynamic control in induction motor field-weakening region," *IEEE Transactions on Power Electronics*, Vol. 35, No. 9, 8860–8866, 2020.

16. Zhang, W. W., F. Xiao, J. L. Liu, Z. Q. Mai, and C. R. Li, "Optimization of maximum torque output in the wide speed range of a PMSM traction control system," *Journal of Power Electronics*, Vol. 20, No. 1, 152–162, 2020.

17. Feng, G. D., C. Y. Lai, Y. Han, and N. C. Kar, "Fast maximum torque per ampere (MTPA) angle detection for interior PMSMs using online polynomial curve fitting," *IEEE Transactions on Power Electronics*, Vol. 37, No. 2, 2045–2056, 2022.

18. Xie, F., C. M. Qiu, and Z. Qian, "Optimal speed-torque control of asynchronous motor for electric cars in the field-weakening region based on voltage vector optimization," *IEEE Transactions on Power Electronics*, Vol. 37, No. 1, 830–842, 2022.

19. Gashtil, H., V. Pickert, D. J. Atkinson, M. Dahidah, and D. Giaouris, "Improved voltage boundary with model-based control algorithm for increased torque in the field weakening region of induction machines," *IEEE Transactions on Transportation Electrification*, Vol. 7, No. 3, 1600–1614, 2021.

20. Wang, B., J. Zhang, Y. Yu, X. Zhang, and D. G. Xu, "Unified complex vector field-weakening control for induction motor high-speed drives," *IEEE Transactions on Power Electronics*, Vol. 36, No. 6, 7000–7011, 2021.

21. Zhang, X. A., G. H. B. Foo, and M. F. Rahman, "A Robust field-weakening approach for direct torque and flux controlled reluctance synchronous motors with extended constant power speed region," *IEEE Transactions on Industrial Electronics*, Vol. 67, No. 3, 1813–1823, 2020.

22. Yu, Z. Y., C. Gan, K. Ni, R. H. Qu, and W. B. Kong, "Dual three-phase flux-modulated switched reluctance motor drive with maximum torque per ampere strategy," *IEEE Transactions on Industry Applications*, Vol. 57, No. 6, 5806–5817, 2021.

23. Levi, E. and M. Y. Wang, "A speed estimator for high performance sensorless control of induction motors in the field weakening region," *IEEE Transactions on Power Electronics*, Vol. 17, No. 3, 365–378, 2002.

24. Jo, G. J. and J. W. Choi, "Robust voltage model flux estimator design with parallel vector compensator for sensorless drive of induction motors," *Journal of Power Electronics*, Vol. 21, No. 1, 126–141, 2021.

25. Wang, Z. Y., W. Sun, and D. Jiang, "Stability analysis and trajectory design of a nonlinear switching system for speed sensorless induction motor drive," *IEEE Transactions on Industrial Electronics*, Vol. 69, No. 6, 5514–5524, 2022.

26. Sun, X. D., L. Chen, and H. B. Jiang, "High-performance control for a bearingless permanent-magnet synchronous motor using neural network inverse scheme plus internal model controllers," *IEEE Transactions on Industrial Electronics*, Vol. 63, No. 6, 3479–3488, 2016.

27. Wang, C., A. Jaidaa, Z. Wang, and L. Lu, "An effective decoupling control with simple structure for induction motor drive system considering digital delay," *Electronics*, 2021, doi: 10.3390/electronics10233048.

28. Han, Y. F., X. Q. Wu, G. F. He, Y. H. Hu, and K. Ni, "Nonlinear magnetic field vector control with dynamic-variant parameters for high-power electrically excited synchronous motor," *IEEE Transactions on Power Electronics*, Vol. 35, No. 10, 11053–11063, 2020.

29. Ye, X. T., Z. B. Yang, and T. Zhang, "Modelling and performance analysis on a bearingless fixed-pole rotor induction motor," *IET Electric Power Applications*, Vol. 13, No. 2, 251–258, 2019.

30. Martinez, J., A. Belahcen, and J. G. Detoni, "A 2D magnetic and 3D mechanical coupled finite element model for the study of the dynamic vibrations in the stator of induction motors," *Mechanical Systems and Signal Processing*, Vol. 66–67, 640–656, 2016.

31. Markovic, N., S. Bjelic, F. Markovic, M. Markovic, and S. Jovic, "Theoretical method for determination of the impact of parasitic torques from the equivalent scheme of induction machines fed by PWM inverter," *Measurement*, 2021, doi: 10.1016/j.measurement.2020.108344.

32. Sun, X. D., L. Chen, and Z. B. Yang, "Overview of bearingless permanent-magnet synchronous motors," *IEEE Transactions on Industrial Electronics*, Vol. 60, No. 12, 5528–5538, 2013.